Threshold switching and electrical self-oscillation in niobium oxide films

Xinjun Liu' , Shuai Li, Sanjoy Kumar Nandi, Dinesh Kumar Venkatachalam, and Robert Glen Elliman

Articles you may be interested in

The role of defects in the electrical properties of NbO2 thin film vertical devices
J. Appl. Phys. **6**, 125006125006 (2016); 10.1063/1.4971818

AIP | Journal of Applied Physics

INTRODUCING INVITED PERSPECTIVES

Ultrafast magnetism and THz spintronics

Authors: Jakob Walowski and Markus Münzenberg

Threshold switching and electrical self-oscillation in niobium oxide films

Xinjun Liu,[1,a)] Shuai Li,[1] Sanjoy Kumar Nandi,[1,2,3] Dinesh Kumar Venkatachalam,[1] and Robert Glen Elliman[1]

[1]*Department of Electronic Materials Engineering, Research School of Physics and Engineering, The Australian National University, Canberra, ACT 2601, Australia*
[2]*Research School of Astronomy and Astrophysics, The Australian National University, Canberra, ACT 2601, Australia*
[3]*Department of Physics, University of Chittagong, Chittagong 4331, Bangladesh*

Electrical self-sustained oscillations have been observed in a broad range of two-terminal systems and are of interest as possible building blocks for bio-inspired neuromorphic computing. In this work, we experimentally explore voltage-controlled oscillations in NbO_x devices with a particular focus on understanding how the frequency and waveform are influenced by circuit parameters. We also introduce a finite element model of the device based on a Joule-heating induced insulator-metal transition. The electroformed device structure is represented by a cylindrical conductive channel (filament) comprised of NbO/NbO_2 zones and surrounded by an Nb_2O_{5-x} matrix. The model is shown to reproduce the current-controlled negative differential resistance observed in measured current-voltage curves, and is combined with circuit elements to simulate the waveforms and dynamics of an isolated Pearson–Anson oscillator. Such modeling is shown to provide considerable insight into the relationship between the material response and device and circuit characteristics. *Published by AIP Publishing.* [http://dx.doi.org/10.1063/1.4963288]

I. INTRODUCTION

Threshold switching devices and self-sustained electrical oscillators have attracted particular attention due to their potential for the applications as selector elements in emerging non-volatile memory and as building blocks for bio-inspired neuromorphic computing, respectively.[1–4] Among these, devices based on metal-oxide-metal (MOM) structures offer the advantage of device simplicity and scalability, and have been used to realize systems of nano-crossbar array memory and coupled nano-oscillators.[3–6] The systems of particular interest in the present study display current-controlled negative differential resistance (CC-NDR), also called threshold switching, due to a thermally induced insulator-metal or metal-insulator transition (IMT/MIT).[7–9] The resistance change is dominated by a thermally transformed volume that changes from an insulating to a metallic state at high temperatures and returns to an insulating state when the temperature is lowered. In device operation, the transition is controlled by local Joule heating and the device switches between the insulating and metallic resistance states at particular voltages. Vanadium dioxide (VO_2) is a well-studied prototypic material for the CC-NDR element in relaxation oscillators[10–16] but unfortunately its low transition temperature (T_{IMT}) ($\sim$340 K) precludes its use in many microelectronics applications, where the expectation is that devices will operate at temperature approaching 400 K. Recent interest has focussed on related IMT materials with higher transition temperatures, including NbO_2 which has a transition temperature of $\sim$1073 K,[17,18] extending the possible temperature range of applications.

Although there are some early reports on NbO_2 self-oscillation,[19,20] Lalevic and Shoga first reported stable and reproducible oscillations with frequency up to $\sim$600 kHz in single crystal NbO_2 and polycrystalline NbO_x films in 1981.[21] Recently, several reports have highlighted the non-linear current–voltage ($I - V$) characteristics of electrically switched NbO_x thin films[22–25] and the occurrence of MHz periodic oscillation signals maintained across two-terminal devices.[7,26,27] Our previous study demonstrated the electrical self-oscillation with a frequency of tens of MHz in a Ti/NbO_x NDR device with low operation voltages, large frequency control range, and long endurance.[26] A unique feature of these IMT-based oscillators is that they do not require any inductive elements or transistors as required in conventional electrical oscillators.[7] The oscillation frequency can also be tuned over several orders of magnitude by controlling the source voltage or load resistance.[5,6] These features are particularly attractive for making scalable, low-power devices.

The threshold switching mechanism in amorphous NbO_x films remains unclear, with recent discussion centering around two mechanisms: one based on the thermally induced IMT in crystalline t-NbO_2;[7,17] and the other, a purely electronic model, based on the temperature dependence of Poole-Frenkel (PF) conduction.[28–30] Both models assume that switching occurs along a filamentary path created during electroforming and results from a reduction in electrical resistivity with the increasing temperature due to local Joule heating. The difference is the basis of the resistivity change, which in one case is a thermally induced IMT and in the other is an increase in trap-assisted carrier transport. Since the IMT is specific to crystalline NbO_2, it has been speculated that a polycrystalline NbO_2 zone or filament is created by the

a)Electronic addresses: tjuxjliu@yahoo.com and xinjun.liu@anu.edu.au

electroforming process and that this is responsible for the IMT response.[31–33] This is not unreasonable given the high local temperatures ($>1073\,$K) associated with the electroforming process, and indeed, it has recently been confirmed experimentally for films subjected to high forming currents.[29,34,35] It is also interesting to note that the limited number of transition metal oxides (TMOs) that exhibit reliable threshold switching (e.g., TiO_x, VO_x, and NbO_x) also have crystalline phases that exhibit thermally induced IMTs.[8] Various combined phase structures of NbO, NbO_2, and Nb_2O_{5-x} have been proposed to result from electroforming,[34] including structures comprised of a NbO/NbO_2 current channel.[24] The threshold switching response will be clearly influenced by such microstructure.

Here, we investigate the self-oscillation behavior of NbO_x threshold switching devices and introduce a finite-element model of threshold switching that accounts for the CC-NDR response of devices and provides the basis for studying the relationship between the materials response and oscillator dynamics. The model is based on a Joule-heating induced IMT in NbO_2, with the electroformed device structure represented by a NbO/NbO_2 current channel (filament) surrounded by an oxygen-deficient Nb_2O_{5-x} matrix. The model is extended to include the effect of circuit elements in a simple Pearson–Anson electrical circuit and shown to capture the periodicity and waveform of device currents and voltages as a function of the circuit parameters. These simulations provide an in-depth understanding of the nature of oxide oscillators and their dependencies.

II. EXPERIMENTAL AND SIMULATION METHOD

A. Devices

Pt/Ti(10 nm)/NbO_x/Pt test structures were employed for this study, as shown in Figure 1(a). To fabricate devices, a 100 nm Si_3N_4 was first deposited on a Si substrate by plasma-enhanced chemical vapour deposition (PECVD) at $300\,°$C. Pt (50 nm) bottom electrodes (BEs) were then deposited on the Si_3N_4 by electron beam evaporation. Note that the Si_3N_4 surface was cleaned *in-situ* by Ar-ion bombardment prior to Pt deposition to obtain good adhesion between Pt and Si_3N_4. (This was checked by the scotch-tape test before and after annealing up to $500\,°$C.) 75 nm thick films of NbO_x oxide were deposited onto the Pt BEs at room temperature using reactive sputtering from a metallic niobium target, in which the stoichiometry was controlled by the ratio of argon to oxygen (18/2 at 20 sccm) at a constant total pressure of 4 mTorr and constant power of 150 W. Patterned top electrodes (150–250 μm in diameter) were then deposited through a shadow mask by e-beam evaporation in a vacuum better than 10^{-6} Torr. These comprised a $\sim$10 nm Ti layer followed by a 50 nm Pt layer to provide more robust contact pads and to protect the Ti from oxidation. After fabrication devices were subjected to a rapid thermal anneal at $300\,°$C for 5 min. Pt/Nb(10 nm)/NbO_x/Pt structure was also fabricated and annealed under the same condition.
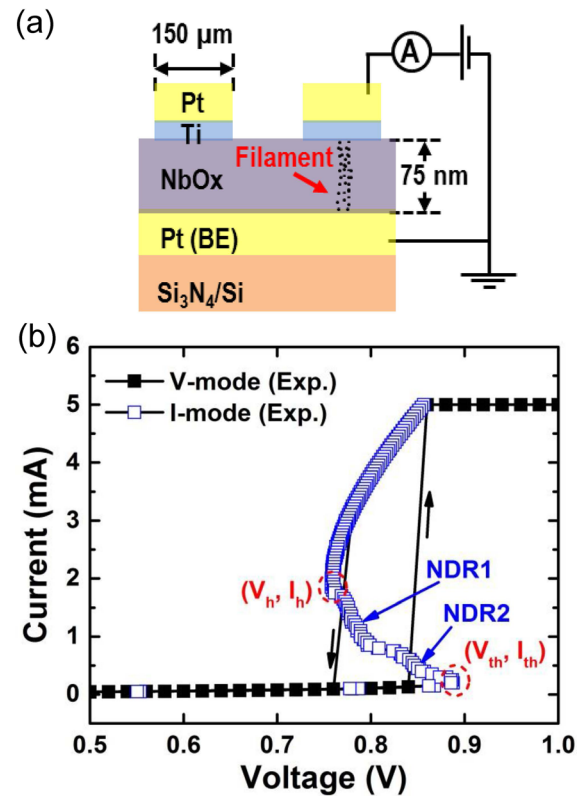

FIG. 1. (a) Schematic of the fabricated Pt/Ti/NbO_x/Pt test devices and the measuring conditions. (b) Measured $I-V$ curves for both voltage- and current-sweeping modes, showing a clear CC-NDR characteristic with multi-NDR properties.

B. Characterization

The stoichiometry of the NbO_x layers was determined by the electron Rutherford backscattering (eRBS) technique[24,36] and X-ray diffraction confirmed that they were amorphous, both as-deposited and after annealing at $300\,°$C.[37] Electrical measurements were carried out in air using an Agilent B1500A semiconductor parameter analyser attached to a Signatone probe station. Rectangular voltage pulses were generated with a Waveform Generator/Fast Measurement Unit (WGFMU) as part of the B1500A analyser, and the resulting electrical response was recorded by monitoring the voltage drop across the 50 Ω resistor using a Tektronix TPS2024B oscilloscope.

C. Numerical calculations

Finite-element simulations of Joule heating in the NbO_x film are performed using the COMSOL Multiphysics software by coupling *electric current* (*ec*) and *heat transfer in solids* (*ht*) physics modules. DC switching characteristics were calculated by assuming an increasing voltage/current sweep with positive sign for insulator-metal transition. Subsequently, the two dimensional axis-symmetric model of the NbO_x film that acted as a resistive element is further coupled with *electrical circuit* (*cir*) module included with the DC supply, load resistor (R_L), and capacitor (C). The full model is solved self-consistently to capture the circuit response to any parameter change.

III. ELECTRICAL SWITCHING AND DYNAMICS PROPERTIES

The as-deposited NbO_x film was amorphous and remained so after annealing.[37] Threshold switching behaviour and electrical self-oscillation were only observed after an initial electroforming step in which the device was subjected to a negative voltage sweep to induce soft breakdown.[26,37] Given that a Ti electrode is used in the present study, it is also important to note that self-oscillation behaviour has been observed in polycrystalline TiO_2 thin films in $Ti/TiO_x/Cr$ device structures.[38] To assess the effect of titanium suboxides in the present case, $Pt/Nb/NbO_x/Pt$ device structures were characterised for comparison. These devices exhibited similar threshold switching and self-oscillation behaviour after an initial electroforming step (see Figure S1 in the supplementary material), suggesting that threshold switching is due to NbO_x.

A. I–V response

The $I-V$ response of Ti/NbO_x devices is shown in Figure 1(b) for both voltage- and current-controlled sweeping modes, clearly highlighting the threshold switching response and CC-NDR. In the low applied current range from 50 to 200 μA, the voltage is observed to increase continuously; the device is in high resistance state, i.e., "*off*" state. When the applied current surpasses the threshold current ($I_{th} \sim 0.2$ mA—labelled B) the voltage starts to decrease continuously, with an onset voltage for the NDR at ~ 0.88 V, called the threshold voltage (V_{th}). This corresponds to the onset of the IMT transition and the device continues to exhibit NDR until the current is increased to the hold current ($I_h \sim 2.1$ mA—labelled D), which corresponds to saturation of the metallic phase volume at ~ 0.75 V, called the hold voltage (V_h). After this, the voltage increases monotonically as the current increases, with the device in a low resistance (metallic) state, i.e., "*on*" state. As indicated in Figure 1(b), multi-NDR regions are evident in the $I-V$ curves, similar to those observed in VO_2 devices.[11,39–41] In the VO_2 case, it was suggested that the emergence of these NDR regions resulted from the progressive development of the IMT in the oxide material, where metallic nano-domains within the oxide matrix grow gradually and semiconducting and metallic domains co-exist in the oxide films.[11,41] Similar effects can be expected in the case of NbO_x films with intrinsic material inhomogeneities after the electroforming step.

B. Self-oscillation

Switching dynamics and the ability to generate self-sustained oscillations were investigated for the Ti/NbO_x device by integrating it into an electrical circuit similar to a Pearson-Anson relaxation oscillator with the MOM device acting as the CC-NDR element.[7,26,42] A schematic diagram of the electrical circuit used for the generation of the IMT/MIT electrical oscillation is shown in Figure 2(a). It consists of a pulsed voltage supply, a load resistor (R_L), a 50 Ω monitoring resistor and the CC-NDR device under test. The input voltage pulse (V_S) and the voltage across the 50 Ω resistor

($V_{50\Omega}$) during voltage excitations were monitored using a Tektronix TPS2024B oscilloscope. The series resistor R_L modifies the Ti/NbO_x IMT dynamics through negative feedback, and to achieve oscillation, the external resistance, $R_L + 50$, should be larger than the critical resistance:[5] $R_C = \frac{V_{th} - V_h}{I_h - I_{th}} \sim 70 \, \Omega$. Load line analysis[26,43] shows that the voltage window for stable oscillation is from $V_{S,min}$ to $V_{S,max}$, where $V_{S,min} = V_{th} + (R_L + 50)I_{th}$ and $V_{S,max} = V_h + (R_L + 50)I_h$.

A 2-μs-long bias pulse with the voltage amplitude in the range of ($V_{S,min}$, $V_{S,max}$) was applied, during which voltage oscillations across the Ti/NbO_x device were observed.[26] With R_L of 1 kΩ, load-line analysis indicates that voltage generation window is (1.1, 2.9) V. Figure 2(b) shows the measured device current ($I_{Device} = I_{50\Omega} = V_{50\Omega}/50$) at various V_S values ranging from 1.0 to 2.8 V. Three features are evident: (a) Sporadic oscillations with an ill-defined period for V_S around 1.17 V, which is the threshold for inducing the IMT in the NbO_2 zone or filament. Interestingly, even when using the same operation conditions, a different number of peaks is observed (see Figure S2 in the supplementary material), an effect related to the stochastic nature of the switching process and intrinsic material inhomogeneities; (b) stable relaxation oscillation for $V_S > 1.17$ V, which is the most interesting feature for many applications;[2–4] and (c) damped oscillations for $V_S \geq 2.6$ V, where the NbO_2 zone tends to remain in the metallic state during the pulse period. This damped oscillation is typical for a circuit with CC-NDR elements when the source voltage is close to the upper limit. These features can also be observed for different V_S with $R_L = 500 \, \Omega$, 2 kΩ, and 4 kΩ, as shown in Figure S3 (supplementary material).

The frequency of the NbO_x oscillator was observed to increase as V_S increased,[5,10,26] with a voltage tuning sensitivity of f_{Osc} from 22.6 MHz/V with R_L of 0.5 kΩ to 2.5 MHz/V with R_L of 4 kΩ. Besides V_S and R_L in this experimental configuration, the frequency was also controlled by the intrinsic device capacitance (C_{Device}) and the parasitic capacitance ($C_{Parasitic}$), where the latter arises from the measurement system, i.e., coaxial cables, the voltage source, and probes.

Figure 2(c) shows typical device current ($I_{Device} = I_{50\Omega} = V_{50\Omega}/50$) oscillations for $V_S = 1.2$ V (2 μs) directly after a measurement of the $I-V$ characteristic in Figure 1(b). This shows stable waveforms with six oscillation periods as a result of repetitive switching and relaxation. The fundamental frequency of the oscillator here is ~ 3.5 MHz. The current waveform in one oscillation period consists of two parts: a rapid current *spike* followed by a slower *decay*. It is expected that each *spike* component is related to the IMT/MIT transition of the threshold switching device, where the device changes between a low-current insulator state and high-current metal state. However, the peak-to-peak amplitudes of the current waveforms ($\Delta I_{peak-to-peak}$) were measured as ~ 0.4 mA, which is $\sim 21\%$ of the difference between the I_{th} and I_h ($\Delta I = I_h - I_{th} = 1.9$ mA). This is not the case in VO_2 devices reported by Kim *et al.*,[13] where the $\Delta I_{peak-to-peak}$ is almost the same as ΔI. This difference is related to the ratio between C_{Device} and $C_{Parasitic}$ in the circuit and will be discussed further in Sec. IV.
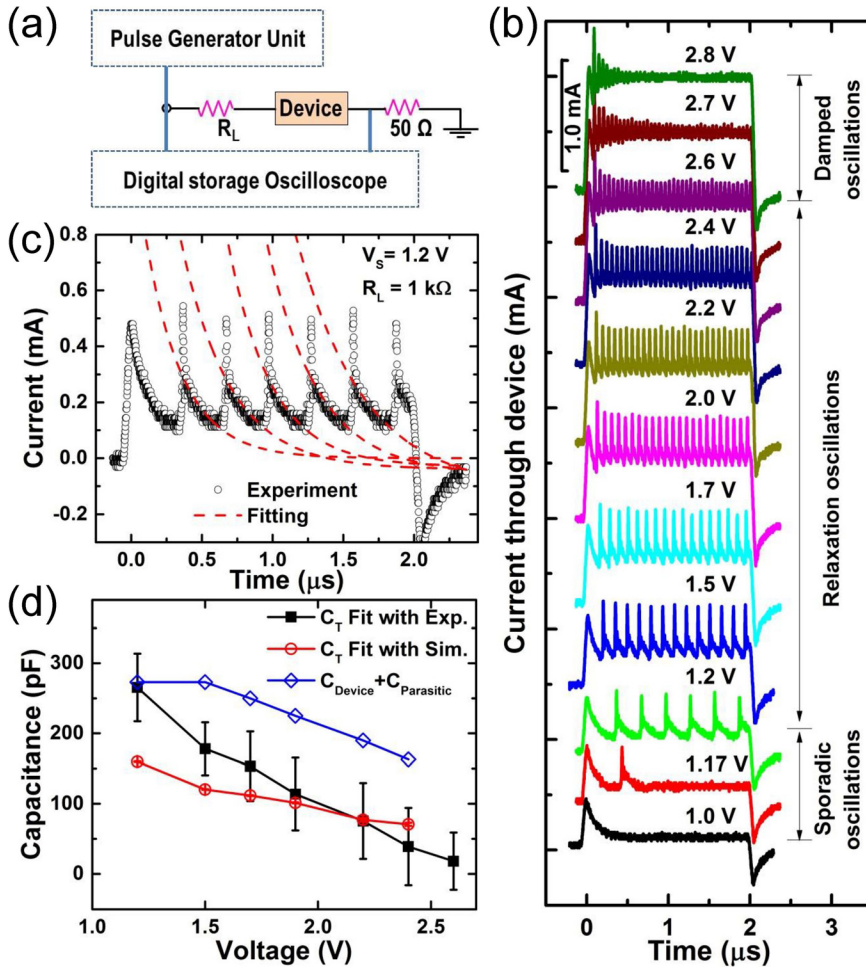
FIG. 2. (a) Schematic of the electrical circuit used to study the dynamics of self-oscillation when exciting the NbO_x device with rectangle voltage pulses. (b) Measured oscillation waveform of the device current (I_{Device}) in the 50 Ω resistor for 2 µs source voltage (V_S) pulses in the range from 1.0 to 2.8 V and a series resistor of 1 kΩ. (c) The *decay* part of the current waveform with fitted exponential decay curves from simple circuit analysis. (d) The total capacitance C_T determined from fits to experimental and simulated waveforms, and the sum of the simulated device capacitance C_{Device} and circuit capacitance $C_{Parasitic}$ as a function of the source voltage.

The *decay* part of the current oscillation can be fitted with an exponential decay curve derived from simple circuit analysis[10,13]

$$I_{Device} \propto V_S \left[1 + \frac{R_D}{R_L + 50} \exp\left(-\frac{t - t_0}{\tau} \right) \right], \quad (1)$$

where I_{Device} is the current across the device, V_s is the source voltage, and $\tau = R_T C_T$ is the time constant of the circuit, where $R_T = \frac{R_D(R_L+50)}{R_D+R_L+50}$ is the overall resistance in the circuit, and C_T is the overall capacitance associated with C_{Device} and $C_{Parasitic}$. In Figure 2(c), the red dashed lines show fits to the data with the exponential decay curve of Equation (1). Based on the fitted results, C_T was estimated as ~265 pF for a bias voltage of 1.2 V and was found to decrease with the increasing voltage, as shown in Figure 2(d). A similar phenomenon of negative differential capacitance has also been observed in VO2 films[13] and interpreted as an increase in the fraction of metallic nano-domains within the switching region with increasing voltage. Further deep experiments are needed to clarify the origin of the phenomenon in the NbO_x devices.

IV. SIMULATION AND DISCUSSION

Pickett and Williams established a simple analytical model of threshold switching based on Joule heating of a volume that undergoes an insulator-to-metal transition, and used a SPICE simulation to obtain good agreement with the experimental measurements of the static and dynamic behaviour of devices.[7] However, a large departure between the experimental and the model I–V curves was observed, especially in the low current region below the threshold voltage.[7] This departure was believed to arise from the most aggressive assumption of their model where the electrical resistance of the insulating phase is linear and temperature independent, and the temperature within the metallic filament is constant. Furthermore, using these simple material and geometric parameters, this model fails to adequately describe our data, in particular, the feature of the NDR region in the static current-sweeping I–V curves (see Figure S4 in supplementary material). To address these limitations and more accurately describe Joule heating and thermal transport between the metallic filament and the surrounding device, a numerical model based on the finite element method is presented for threshold switching.

To reproduce the $I - V$ curves in Figure 1(b), a two dimensional (2-D) axis-symmetric finite element simulation model was solved self-consistently in a time-dependent solver. In relation to our micro-meter sized devices with 75 nm thick films and the high compliance current (~20 mA) forming process,[37] the model considers a NbO/NbO2 current channel (filament) surrounded by oxygen-deficient Nb2O5−x as the simulated cell, where the effective NbO2 zone is a small active region with 100 nm diameter and 30 nm
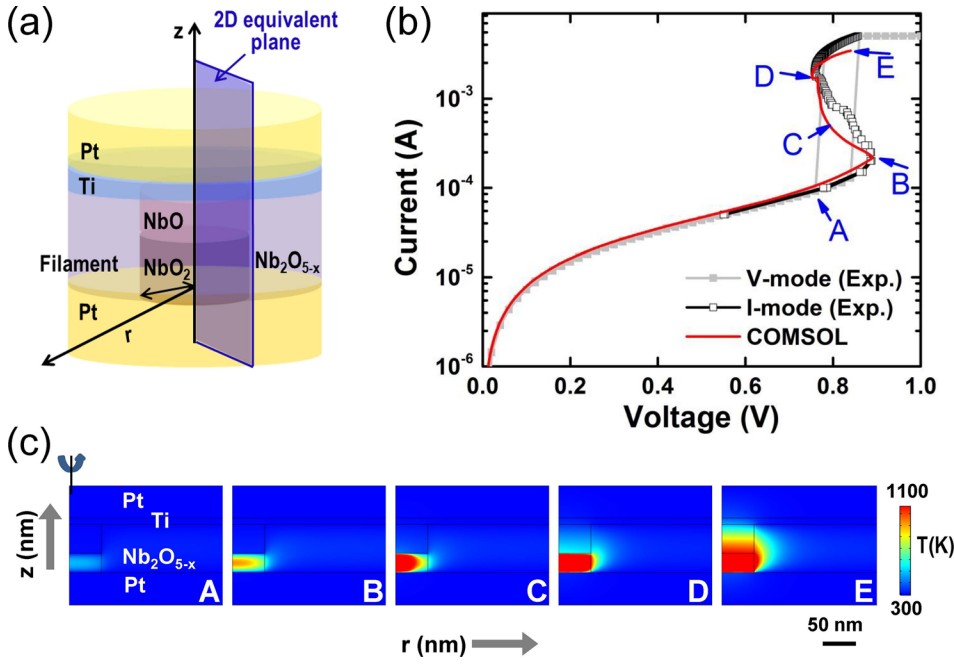
FIG. 3. (a) Geometry of the simulated device structure assuming a cylindrical conductive channel (filament) comprised of NbO/NbO$_2$ zones and surrounded by an Nb$_2$O$_{5-x}$ matrix. (b) The comparison of simulated and experimental I–V characteristics of Pt/Ti/NbO$_x$/Pt devices. (c) Calculated 2-D maps of temperature for states A, B, C, D, and E as depicted in the I–V curve of the simulation results. The red color represents the high-temperature metallic regions during the IMT.

thickness, as shown in Figure 3(a). The threshold switching response of NbO$_2$ is assumed to result from a thermally induced IMT as proposed by Pickett and Williams.[7] The time-dependent heat equation is solved, along with the continuity equation for temperature T and potential V,[24,44] i.e.,

$$\rho_m C_p \partial T / \partial t - \nabla k \nabla T = J^2/\sigma, \tag{2}$$

$$\nabla J = \nabla \sigma \nabla V = 0, \tag{3}$$

where ρ_m, C_p, k, J, and σ denote mass density, heat capacity, thermal conductivity, local current density, and electric conductivity, respectively. The k and σ values of NbO$_2$ film depend on device temperature and its conduction state. Simply, we use $k_{insulator} = 0.07$, $k_{metal} = 1.5$ W m^{-1}K^{-1}, and $\sigma_{insulator} = \sigma_o \exp(-E_{AC}/k_B T)$, $\sigma_{metal} = 1 \times 10^4$ Ω^{-1}m^{-1}. Here, σ_o is a pre-exponential factor, and E_{AC} is the activation energy for carrier transport. We further assumed that the Nb$_2$O$_{5-x}$ zone represented the high resistance state of the memory,[45] and that the temperature dependence of k and σ were given by: $\sigma_{Nb_2O_5} = \sigma_o \exp(-E_{AC}/k_B T)$ and $k_{Nb_2O_5} = k_{th0}(1 + \lambda(T - T_0))$, where $\sigma_o = 100$ Ω^{-1}m^{-1}, $E_{AC} = 0.048$ eV, $k_{th0} = 0.035$ W m^{-1}K^{-1}, and $\lambda = 0.01$ K^{-1}. The k and σ values of the NbO zone represented the low resistance state of the memory, and were assumed as $\sigma_{NbO} = 7.5 \times 10^4$ Ω^{-1}cm^{-1} and $k_{NbO} = 10$ W m^{-1}K^{-1}.[45] For the k and σ values of Pt and Ti and other used material parameters such as mass density and heat capacity, we used the build-in material parameters in COMSOL software.

The T_{IMT} for thermally induced phase transitions in transition metal oxides can differ during heating and cooling branches.[16] However, no such hysteresis is reported for NbO$_2$ films.[17] To simplify the analysis, we therefore assumed the same transition temperature in the calculation, with the IMT transition modelled by temperature-dependent thermal and electrical conductivities that vary between those of the insulating and metallic phases over a temperature range of 100 K,

centered at the nominal transition temperature of 1073 K. These parameters were chosen to match the published data on the IMT in NbO$_2$.[7,24] This allowed a quantitative analysis of field and temperature contributions and accounts accurately for the CC-NDR characteristics of the DC response.[24,46,47]

A. *I–V* characteristics

The calculated $I - V$ characteristics for the best fit of the model to the experimental data are shown in Figure 3(b). Both the low and high current regions are matched reasonably well except a deviation in the multi-NDR region. The on/off ratio for the current jump across the transition is around one order of magnitude, which is close to the resistance change across the thermal transition in NbO$_2$. The threshold and hold voltage points are ($V_{th} \sim 0.89$ V; $I_{th} \sim 0.2$ mA) and ($V_h \sim 0.74$ V; $I_h \sim 1.6$ mA), respectively, where only the hold current is less than the experimental data (2.1 mA). Hence, this model can be used as a predictive tool for circuit design as well as for simulating the parametric behaviour of oxide threshold switching. Figure 3(c) shows the calculated 2-D map of temperature for states A, B, C, D, and E as labelled in Figure 3(b). Initially, at low biases, the device is resistive and the current conducts through the NbO$_2$ zone, then the temperature increases with the increasing current due to Joule heating (A-B in Figure 3(c)). As the device current increases above I_{th} (B in Figure 3(c)), the conductivity of the filament decreases and the local IMT is induced in the central hot spot of NbO$_2$ zone, as shown in the red color region, which results in the CC-NDR shown in the $I - V$ curve. A complete metallic NbO$_2$ zone emerged around I_h (D in Figure 3(c)), and as the current increases further, the NbO$_2$ zone remains in the metallic state, and the temperature increases further (D-E in Figure 3(c)).

The I–V curves for different devices show some variability due to the simple device structures employed (i.e.,

direct probing onto contact pads) and due to the statistical variability in the electro-forming process. The resulting *I–V* curves can be fitted using the proposed IMT model by changing the "effective" geometry of the filament (i.e., the diameter and relative thickness of the filamentary oxide layers), as might be expected to result from different electroforming conditions. Indeed, the model has general applicability and can also be used to model devices with small active regions such as that in Pickett's paper.[7] From an experimental perspective, improvements in uniformity have recently been demonstrated for Pt/NbO$_x$/TiN structures using more controlled electroforming (series resistance to reduce current overshoot).

Alternative models of the NDR response in NbO$_x$ have also recently been proposed.[28–30] These are based on the temperature and field dependence of PF conduction rather than the thermally induced IMT in crystalline t-NbO$_2$.[7,17] However, the calculated NDR response in these models critically depends on the assumed temperature and field dependence of the film conductivity as well as accurate modelling of local Joule heating. The uncertainty associated with these assumptions and the sensitivity of the calculated temperature rise to such parameters makes it difficult to distinguish between the various PF and IMT models. For example, the current IMT model can also generate the NDR response reported by Funck.[30] Clearly, new experiments are required to identify the specific NDR mechanism in NbO$_x$.

B. Oscillation characteristics

To simulate the dynamics of the device in an oscillator circuit, including the frequency and waveform of the device current, the model was extended to include circuit elements as shown in the schematic of Figure 4(a). To match the current oscillation curves, the parameters obtained by fitting the $I - V$ measurement of Figure 3(b) were used and the value of C_{Device} and $C_{Parasitic}$ were adjusted. Here, the $C_{Parasitic}$ is marked in the circuit schematic, and plays an important role in determining the oscillation waveform.

As shown in Figure 4(b) for the case of $V_S = 1.2$ V (2 μs) and $R_L = 1$ kΩ, the model captures the periodicity and waveform of the oscillations and reproduces the experimental behaviour very well. The optimal value of C_{Device} is 240 pF, which is close to the value determined from complex impedance spectra reported for micro-sized NbO$_x$ devices,[48] and the optimal value of $C_{Parasitic}$ is 33 pF, which is comparable to the measured open circuit capacitance of the measuring system. The calculations show that the current waveform is sensitive to the value of $C_{Parasitic}$. For example, for $C_{Parasitic} = 0$, the current *spike* disappears, resulting in a sawtooth waveform with the same fundamental frequency, as shown by the green line included in Figure 4(b).

An expanded view of the current *spike* region is shown in Figure 4(c). Both the experimental and calculated *off-to-on*-transition times are $\Delta t_{ON} = 14$ ns, which is consistent with a previous experimental report ($\sim$22 ns) (Ref. 49) but
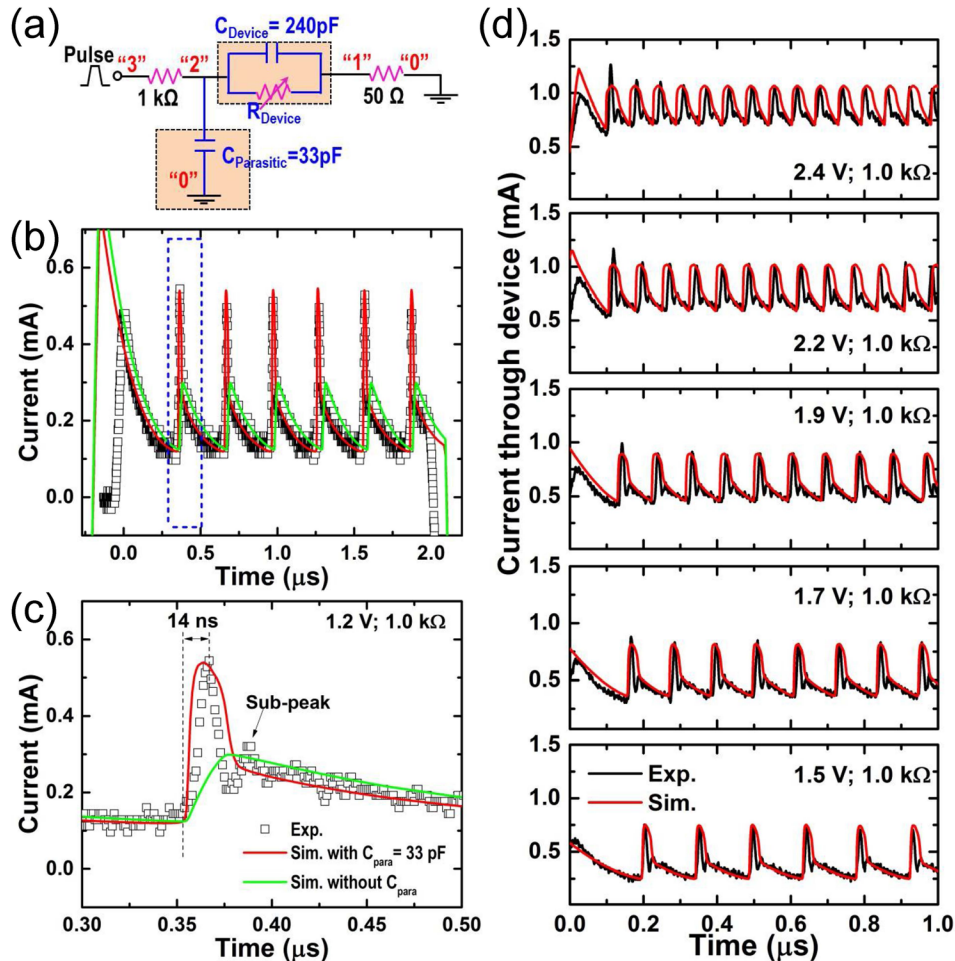

FIG. 4. (a) Schematic of the electrical circuit used in simulation to study the dynamics of self-oscillations. (b) Measured (black squares) and simulated (red curves) oscillation waveforms of the current through the 50 Ω resistor for a source voltage of $V_S = 1.2$ V (2 μs) and the series resistance of $R_L = 1$ kΩ. The green lines show the simulation data for $C_{Parasitic} = 0$ for comparison, where no current *spike* was observed in the current waveform. (c) Magnification of the dashed rectangle region in (b). (d) Measurements (black curves) and simulation (red curves) of time traces of the current through the device when excited with source voltages ranging from 1.5 V (bottom) to 2.6 V (top) with 1 kΩ series.

the two orders of magnitude larger than that ($\sim$700 ps) reported by Pickett and Williams.[7] This highlights the effect of the measurement system and device structure on the observed rise time. Measurement of the ***on*-to-*off*-transition** time is complicated in the present case by a sub-peak in the current oscillation which appears to result from the multi-NDR regions in the $I - V$ curves in Figure 1(b). An estimate of $\sim$4.0 pJ for the total energy input during ***on*-switching** can be obtained by noting that the voltage across the device was $\sim$0.9 V and that numerical integration of the measured current over the transition time is $\sim$4.4 pC. This is more than one order of magnitude larger than that obtained from Pickett's experiments due to the energy consumption from the intrinsic parallel capacitance.[7]

To match the measured pulse characteristics for other source voltages above 1.5 V, first we fixed the two capacitances as $C_{Device} = 240$ pF and $C_{Parasitic} = 33$ pF. As shown in Figure S5 (supplementary material), the simulated current waveforms deviate from the experimental data above 1.7 V, i.e., the frequency and waveform of simulated curves do not match the experimental data for increasing source voltage. Considering the phenomenon of negative differential capacitance shown in Figure 2(d), we have adjusted the value of C_{Device} and $C_{Parasitic}$ to match the measured oscillation waveforms for other source voltages in the range from 1.5 to 2.4 V, as shown in Figure 4(d). The sum of $C_{Device} + C_{Parasitic}$ was plotted in Figure 2(d) as a function of source voltages.

Moreover, we fitted our calculated waveforms with the exponential decay curve of Equation (1) from simple circuit analysis. Then the obtained C_T for different V_S shows the same trend as that from the experimental data, as shown in Figure 2(d). However, these calculated C_T values are not equal to the sum of $C_{Device} + C_{Parasitic}$, due to circuit dynamics. For the voltage pulse of 2.6 V, the simulated device current does not show oscillation behavior: this is due to the fact that the voltage exceeds the upper limit of the stable oscillation window, which is limited to the voltage range 1.1 to 2.5 V from load-line analysis of the calculated $I - V$ curve in Figure 3(b). This model can also be used to simulate other measured pulse characteristics for different source voltages with of $R_L = 500\ \Omega$, 2 kΩ, and 4 kΩ, as can be seen in Figure S6 (supplementary material).

C. Voltage/current waveforms and limit cycles

To better understand the device behaviour and the dynamics associated with oscillations, Figure 5(a) shows the relationship between the device voltage V_{Device} and various current components for a single oscillation period in terms of simulation data for $V_S = 1.2$ V. The latter include the current due to the resistance of the device (I_{R_device}), the current due to the capacitance of device (I_{C_device}), the total device current I_{Device}, and the current due to parasitic capacitance ($I_{C\_parasitic}$). The sequential charging and discharging stages are evident in the V_{Device} trace which is related to the low and high current regions of the I_{R_device} signal. Note that I_{R_device} is positive while I_{C_device} is negative, and the sum of the two currents is the current through the device: I_{Device}

$= I_{R\_device} + I_{C\_device}$. This is the origin of the deviation mentioned above where the $\Delta I_{peak-to-peak}$ is less than the current difference between the I_{th} and I_h. The oscillation waveforms for the total device current have a roughly trapezoidal shape, which is also observed in the other reported experiments.[6,7,50] The current through the parasitic capacitance, $I_{C\_parasitic}$ is also negative due to the charging and discharging of $C_{Parasitic}$, which also influences the waveform of I_{Device}. As a consequence, the peak of I_{Device} occurs concurrently with the minimum of $I_{C\_parasitic}$, but it has $\sim$6 ns delay compared with the maximum of I_{R_device}, as shown in Figure 5(a). Consequently, the oscillation frequency, the waveform of I_{Device}, the peak-to-peak current amplitude, and even the ***off*-to-*on*-transition** time are affected by C_{Device} and $C_{Parasitic}$, as discussed later.

Replotting the I_{Device}–V_{Device} response for $V_S = 1.2$ V defines a limit cycle as shown by the red line in Figure 5(b), which is a characteristic of self-sustained oscillators.[27,51,52] The I_{R_device}–V_{Device} response (blue line) is also plotted in Figure 4(b), and is shown to roughly match the hysteresis region of the voltage sweeping $I - V$ curves (dashed line). In relation to the current sweeping $I - V$ curves (dotted line), four characteristic points for a cycle of I_{R_device} oscillation are marked in Figure 5(b), which corresponds to those in Figure 3(b). Region B-E represents the IMT, E-D corresponds to the device in a metallic state, D-A represents the MIT, and A-B corresponds to the device in its insulating state. The oscillation mechanism can then be described as follows: (a) Starting from the threshold-bias point B, the current rises to the ***on*-state** point E upon switching as a result of the total capacitance (C_T) in the circuit; (b) the current decreases to point D of the $I_{R\_device} - V_{Device}$ characteristic as the capacitance discharges, and then, the current falls to the ***off*–state** point A due to the MIT; (c) then the voltage increases as the capacitance charges, and a new cycle of oscillation begins once the threshold-bias point B is reached, where the conditions for the onset of oscillating behaviour are satisfied again.

The corresponding four characteristic points are also marked in Figure 5(a) to determine the IMT/MIT transition time. The rise time of 14 ns from B to E in the simulation of I_{R_device} and I_{Device} is consistent with the experimental value as shown in Figure 4(c). Here, each ***spike*** component can be related to the IMT(B-E), metal (E-D), and MIT (D-A), while each ***decay*** component can be related to the insulator state (A-B) of the device. The corresponding time was defined as t_{IMT}, t_{metal}, t_{MIT}, and $t_{insulator}$. For the case of $V_S = 1.2$ V and $R_L = 1$ kΩ, the oscillation period is $T_{Osc} = t_{IMT} + t_{metal} + t_{MIT} + t_{insulator} = 14 + 17 + 10 + 266 = 307$ ns. All four stages can be tuned by appropriate control of the bias voltage, a series resistor, and an external capacitance. The oscillation frequency f_{Osc} can be tuned accordingly.

Similarly, the I_{Device}–V_{Device} response for $V_S = 2.2$ V and $R_L = 1$ kΩ, also defines a limit cycle as shown by the red line in Figure 5(c). In relation to the voltage sweeping $I - V$ curves (dashed line), the I_{R_device}–V_{Device} response represents a deformed hysteresis region as shown by the blue line in Figure 5(c), which is a dynamic feature due to the high frequency. Note that if the $C_{Parasitic} = 0$, the limit cycle
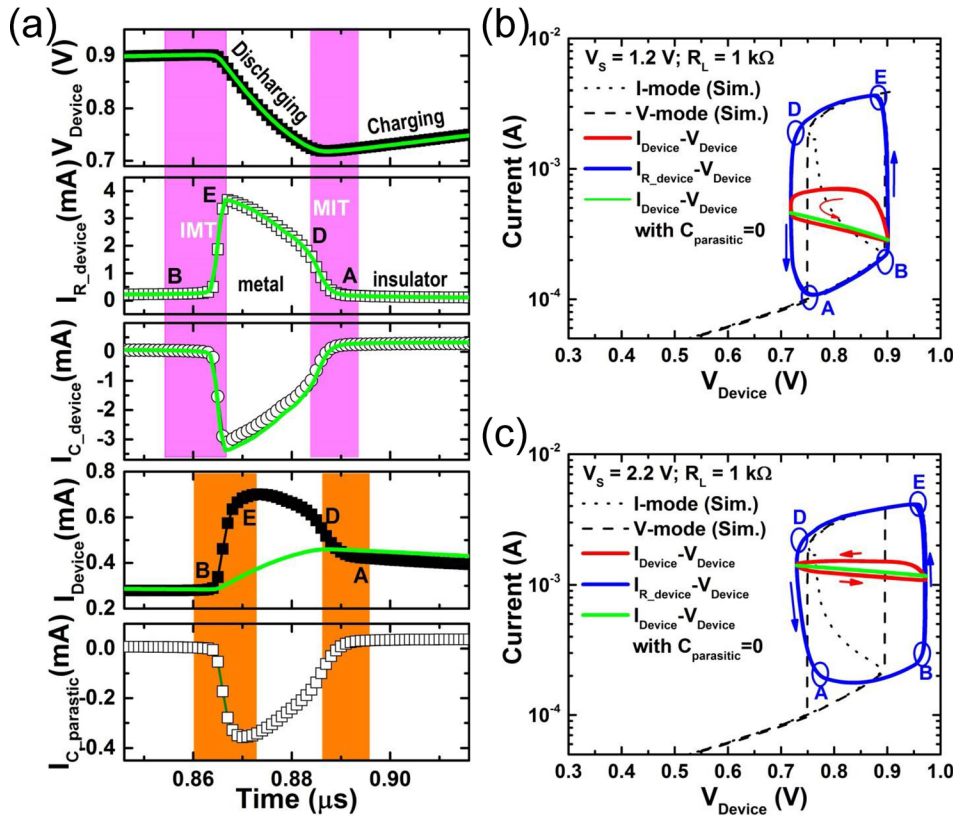
FIG. 5. (a) Calculated device voltage, V_{Device}, and related current components: I_{R_device}, I_{C_device}, I_{Device}, and $I_{C\_parasitic}$ for a source voltage of $V_S = 1.2$ V and load resistance of $R_L = 1$ kΩ. (b) and (c) Show the limit cycles of $I_{Device} - V_{Device}$ (red lines) for $V_S = 1.2$ V and 2.2 V, respectively. The green lines show the simulation data of $I_{Device} - V_{Device}$ with $C_{Parasitic} = 0$, where the limit cycles collapse to straight lines. The blue lines show the $I_{R\_device} - V_{Device}$ characteristics. The black lines show the $I \sim V$ response of the device under voltage-controlled (dashed) and current-controlled (dotted) operation for comparison.

collapses to a straight line for both $V_S = 1.2$ V and 2.2 V case with $R_L = 1$ kΩ, as shown by the green lines in Figures 5(b) and 5(c).

D. Capacitance dependence on $\Delta I_{peak-to-peak}$ and frequency

The tunability of this Ti/NbO$_x$ oscillator, including the effect of device and parasitic capacitances on the operating frequency, is explored through two sets of simulations: (1) C_{Device} is varied from 1 pF to 2 nF and the other parameters are kept constant ($V_S = 1.2$ V, $R_L = 1$ kΩ, and $C_{Parasitic} = 33$ pF); (2) $C_{Parasitic}$ is varied from 1 pF to 5 nF and the other parameters are kept constant ($V_S = 1.2$ V, $R_L = 1$ kΩ, and $C_{Device} = 240$ pF). Results show that both the oscillation wave shape and frequency depend strongly on C_{Device} and $C_{Parasitic}$. Figures 6(a) and 6(b) show the current-time characteristics of simulated, self-sustained oscillations for various capacitance values, where the effects of capacitance can be clearly observed. The peak-to-peak amplitudes of the total device current ($\Delta I_{peak-to-peak}$) decrease significantly when C_{Device} reaches 500 pF (Figure 6(a)), since a larger device capacitance stores and discharges more charge. By increasing C_{Device}, I_{C_device} increases accordingly and $\Delta I_{peak-to-peak}$ decreases. In contrast, $\Delta I_{peak-to-peak}$ increases significantly when $C_{Parasitic}$ changes from 1 pF to 1 nF (Figure 6(b)). Finally, $\Delta I_{peak-to-peak}$ increases proportionally with the ratio of $C_{Parasitic}$ and C_{Device} and then tends to saturate, as shown in Figure 6(c).

It is believed that the transition between the insulating and the metallic phase in NbO$_2$ results from a thermally induced Mott-Peierls transition in which the NbO$_2$ lattice

undergoes a structural transition from a distorted (insulating) rutile structure at low temperatures to an undistorted (metallic) rutile structure at high temperatures.[53] The physical transition times in a nanoscale NbO$_2$ device between **on** and **off** states have been reported to be ~700 ps for the IMT and 2.3 ns for MIT,[7] which indicates that the maximum achievable frequency for these oscillators is expected to be ~GHz. However, the oscillation frequency is determined by the resistor-capacitor time constant associated with charging/discharging, and in most cases, the peak frequency is limited by $C_{Parasitic}$ and C_{Device}. Figure 6(d) indicates that the frequency is inversely proportional to the sum of $C_{Parasitic}$ and C_{Device}. To increase the frequency, clearly both the $C_{Parasitic}$ and C_{Device} should be reduced. This suggested as the advantage of nanoscale devices for high-frequency operation.

V. CONCLUSION

The electrical self-oscillation behaviour of an NbO$_x$ CC-NDR device was investigated experimentally and with reference to a finite element model of the switching response based on a thermally induced IMT. Room temperature electrical oscillation was demonstrated for a circuit containing the NbO$_x$ device, and shown to be directly related to the presence of the NDR region in the $I - V$ characteristic of the device operated in the current mode. Devices were further shown to display sporadic, relaxation, and damped oscillations depending on the applied voltage and series resistance. A Joule-heating induced electro-thermal threshold switching model based on the finite element method was presented and shown to reproduce the $I - V$ characteristic of the device. Based on this model, the switching dynamics of the electrical
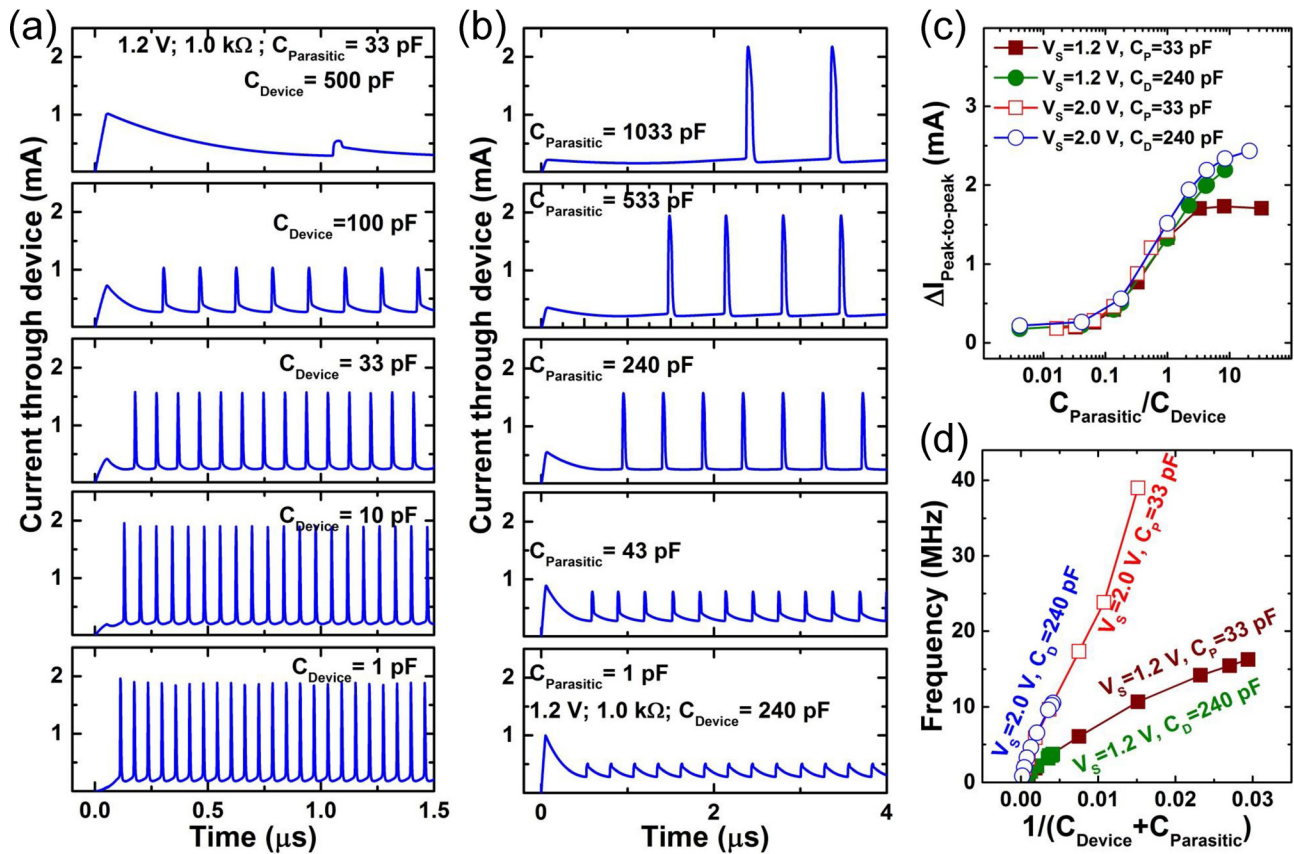
FIG. 6. (a) Waveforms of I_{Device} as a function of the device capacitance C_{Device}, and (b) as a function of the parasitic capacitance $C_{Parasitic}$. (c) The dependence of the peak-to-peak device current on the ratio of $C_{Parasitic}/C_{Device}$. (d) The dependence of the oscillation frequency on the sum of C_{Device} and $C_{Parasitic}$.

circuit which included the CC-NDR device were investigated. The waveform of the device voltage and current were discussed in detail with reference to the model predictions. The model highlighted the role of parasitic and device capacitance in controlling the oscillation frequency and current amplitude. Finally, it is expected that physics-based finite element models can be used to explore oscillator coupling and associated synchronization behaviour.

SUPPLEMENTARY MATERIAL

See supplementary material for the complete experimental and simulated oscillation waveforms of the studied NbO$_x$ devices.

ACKNOWLEDGMENTS

[1]J. J. Yang, D. B. Strukov, and D. R. Stewart, Nat. Nanotechnol. **8**, 13 (2013).

[2]S. D. Ha, J. Shi, Y. Meroz, L. Mahadevan, and S. Ramanathan, Phys. Rev. Appl. **2**, 064003 (2014).

[3]S. Datta, N. Shukla, M. Cotter, A. Parihar, and A. Raychowdhury, in *Proceedings of 51st ACM/EDAC/IEEE Design Automation Conference (DAC)* (2014), pp. 1–6.

[4]M. D. Pickett, G. Medeiros-Ribeiro, and R. S. Williams, Nat. Mater. **12**, 114 (2013).

[5]N. Shukla, A. Parihar, E. Freeman, H. Paik, G. Stone, V. Narayanan, H. Wen, Z. Cai, V. Gopalan, and R. Engel-Herbert, Sci. Rep. **4**, 4964 (2014).

[6]T. C. Jackson, A. Sharma, J. Bain, J. Weldon, and L. Pileggi, IEEE J. Emerging Sel. Top. Circuits Syst. **5**, 230 (2015).

[7]M. D. Pickett and R. S. Williams, Nanotechnology **23**, 215202 (2012).

[8]Z. Yang, C. Ko, and S. Ramanathan, Annu. Rev. Mater. Res. **41**, 337 (2011).

[9]N. Shukla, T. Joshi, S. Dasgupta, P. Borisov, D. Lederman, and S. Datta, Appl. Phys. Lett. **105**, 012108 (2014).

[10]Y. W. Lee, B.-J. Kim, J.-W. Lim, S. J. Yun, S. Choi, B.-G. Chae, G. Kim, and H.-T. Kim, Appl. Phys. Lett. **92**, 162903 (2008).

[11]J. Leroy, A. Crunteanu, J. Givernaud, J.-C. Orlianges, C. Champeaux, and P. Blondy, Int. J. Microwave Wireless Technol. **4**, 101 (2012).

[12]J. Sakai, J. Appl. Phys. **103**, 103708 (2008).

[13]H.-T. Kim, B.-J. Kim, S. Choi, B.-G. Chae, Y. W. Lee, T. Driscoll, M. M. Qazilbash, and D. Basov, J. Appl. Phys. **107**, 023702 (2010).

[14]M. S. Mian, K. Okimura, and J. Sakai, J. Appl. Phys. **117**, 215305 (2015).

[15]A. Beaumont, J. Leroy, J.-C. Orlianges, and A. Crunteanu, J. Appl. Phys. **115**, 154502 (2014).

[16]S. Kumar, M. D. Pickett, J. P. Strachan, G. Gibson, Y. Nishi, and R. S. Williams, Adv. Mater. **25**, 6128 (2013).

[17]R. Janninck and D. Whitmore, J. Phys. Chem. Solids **27**, 1183 (1966).

[18]A. B. Posadas, A. O'Hara, S. Rangan, R. A. Bartynski, and A. A. Demkov, Appl. Phys. Lett. **104**, 092901 (2014).

[19]D. Geppert, Proc. IEEE **51**, 223 (1963).

[20]K. Chopra, Proc. IEEE **51**, 941 (1963).

[21]B. Lalevic and M. Shoga, Thin Solid Films **75**, 199 (1981).

[22]X. Liu, S. M. Sadaf, M. Son, J. Shin, J. Park, J. Lee, S. Park, and H. Hwang, Nanotechnology **22**, 475702 (2011).

[23]X. Liu, S. M. Sadaf, M. Son, J. Park, J. Shin, W. Lee, K. Seo, D. Lee, and H. Hwang, IEEE Electron Device Lett. **33**, 236 (2012).

[24]X. Liu, S. K. Nandi, D. K. Venkatachalam, K. Belay, S. Song, and R. G. Elliman, IEEE Electron Device Lett. **35**, 1055 (2014).

[25]W. Yuhan, R. B. Comes, S. A. Wolf, and L. Jiwei, IEEE J. Electron Devices Soc. **4**, 11 (2016).

[26]S. Li, X. Liu, S. K. Nandi, D. K. Venkatachalam, and R. G. Elliman, Appl. Phys. Lett. **106**, 212902 (2015).

[27]A. Ascoli, S. Slesazeck, H. Mahne, R. Tetzlaff, and T. Mikolajick, IEEE Trans. Circuits Syst. I Regul. Pap. **62**, 1165 (2015).

[28]S. Slesazeck, H. Mähne, H. Wylezich, A. Wachowiak, J. Radhakrishnan, A. Ascoli, R. Tetzlaff, and T. Mikolajick, RSC Adv. **5**, 102318 (2015).

[29]G. A. Gibson, S. Musunuru, J. Zhang, K. Vandenberghe, J. Lee, C.-C. Hsieh, W. Jackson, Y. Jeon, D. Henze, Z. Li, and R. S. Williams, Appl. Phys. Lett. **108**, 023505 (2016).

[30]C. Funck, S. Menzel, N. Aslam, H. Zhang, A. Hardtdegen, R. Waser, and S. Hoffmann-Eifert, Adv. Electron. Mater. **2**, 1600169 (2016).

[31]F. Chudnovskii, L. Odynets, A. Pergament, and G. Stefanovich, J. Solid State Chem. **122**, 95 (1996).

[32]S. Shin, T. Halpern, and P. Raccah, J. Appl. Phys. **48**, 3150 (1977).

[33]J. Park, E. Cha, I. Karpov, and H. Hwang, Appl. Phys. Lett. **108**, 232101 (2016).

[34]B. Boiko, P. Pancheha, V. Kopach, and Y. L. Pozdeev, Thin Solid Films **130**, 341 (1985).

[35]J. Lee, E. Cha, Y. Kim, B. Chae, J. Kim, S. Lee, H. Hwang, and C. Park, Micron **79**, 101 (2015).

[36]M. Vos, X. Liu, P. L. Grande, S. K. Nandi, D. K. Venkatachalam, and R. G. Elliman, Nucl. Instrum. Methods Phys. Res., Sect. B **340**, 58 (2014).

[37]S. Li, X. Liu, S. Nandi, D. Venkatachalam, and R. Elliman, in *Proceedings of 2014 Conference on Optoelectronic and Microelectronic Materials Devices (COMMAD)* (2014), p. 138–140.

[38]G. Taylor and B. Lalevic, Solid-State Electron. **19**, 669 (1976).

[39]Z. Yang, C. Ko, and S. Ramanathan, J. Appl. Phys. **108**, 073708 (2010).

[40]Y. Chang, C. Koo, J. Yang, Y. Kim, D. Kim, J. Lee, T. Noh, H.-T. Kim, and B. Chae, Thin Solid Films **486**, 46 (2005).

[41]J. Rozen, R. Lopez, R. F. Haglund, and L. C. Feldman, Appl. Phys. Lett. **88**, 081902 (2006).

[42]S. Pearson and H. S. G. Anson, Proc. Phys. Soc. London **34**, 204 (1921).

[43]P. E. Schmidt and R. C. Callarotti, J. Appl. Phys. **55**, 3144 (1984).

[44]C. Hermes, M. Wimmer, S. Menzel, K. Fleck, G. Bruns, M. Salinga, U. Bottger, R. Bruchhaus, T. Schmitz-Kempen, and M. Wuttig, IEEE Electron Device Lett. **32**, 1116 (2011).

[45]X. Liu, S. Nandi, D. Venkatachalam, S. Li, K. Belay, and R. Elliman, in *Proceedings of 2014 Conference on Optoelectronic and Microelectronic Materials Devices (COMMAD)* (2014), pp. 280–282.

[46]S. K. Nandi, X. Liu, D. K. Venkatachalam, and R. G. Elliman, J. Phys. D: Appl. Phys. **48**, 195105 (2015).

[47]S. K. Nandi, X. Liu, D. K. Venkatachalam, and R. G. Elliman, Appl. Phys. Lett. **107**, 132901 (2015).

[48]H. Wylezich, H. Mähne, J. Rensberg, C. Ronning, P. Zahn, S. Slesazeck, and T. Mikolajick, ACS Appl. Mater. Interfaces **6**, 17474 (2014).

[49]S. Kim, X. Liu, J. Park, S. Jung, W. Lee, J. Woo, J. Shin, G. Choi, C. Cho, S. Park, D. Lee, E. Cha, B. Lee, H. Lee, S. Kim, S. Chung, and H. Hwang, in *Symposium on Very Large Scale Integration Technology (VLSIT)* (2012), pp. 155–156.

[50]Q. Gu, A. Falk, J. Wu, L. Ouyang, and H. Park, Nano Lett. **7**, 363 (2007).

[51]S. Lavizzari, D. Ielmini, and A. L. Lacaita, IEEE Trans. Electron Devices **57**, 1838 (2010).

[52]A. Cywar, F. Dirisaglik, M. Akbulut, G. Bakan, S. Steen, H. Silva, and A. Gokirmak, IEEE Electron Device Lett. **32**, 1486 (2011).

[53]A. O'Hara, T. N. Nunley, A. B. Posadas, S. Zollner, and A. A. Demkov, J. Appl. Phys. **116**, 213705 (2014).